

Central role of nitric oxide in ozone production in the upper tropical troposphere over the Atlantic Ocean and West Africa

Ivan Tadic¹, Clara M. Nussbaumer¹, Birger Bohn², Hartwig Harder¹, Daniel Marno¹, Monica Martinez¹, Florian Obersteiner³, Uwe Parchatka¹, Andrea Pozzer^{1,4}, Roland Rohloff¹, Martin Zöger⁵, Jos Lelieveld^{1,6} and Horst Fischer¹

- 5 ¹Atmospheric Chemistry Department, Max Planck Institute for Chemistry, Mainz, Germany
²Institute of Energy and Climate Research, IEK-8: Troposphere, Forschungszentrum Jülich GmbH, Jülich, Germany
³Karlsruhe Institute of Technology, Karlsruhe, Germany
⁴Earth System Physics section, The Abdus Salam International Centre for Theoretical Physics, Trieste, Italy
⁵Flight Experiments, German Aerospace Center (DLR), Oberpfaffenhofen, Germany
10 ⁶Climate and Atmosphere Research Center, The Cyprus Institute, Nicosia, Cyprus

Correspondence: Ivan Tadic (i.tadic@mpic.de) or Horst Fischer (horst.fischer@mpic.de)

Abstract. Mechanisms of tropospheric ozone (O₃) formation are generally well understood. However, studies reporting on net ozone production rates (NOPRs) directly derived from in situ observations are challenging, and are sparse in number. To
15 analyze the role of nitric oxide (NO) in net ozone production in the upper tropical troposphere above the Atlantic Ocean and the West African continent, we present in situ trace gas observations obtained during the CAFE-Africa (Chemistry of the Atmosphere: Field Experiment in Africa) campaign in August and September 2018. The vertical profile of in situ measured NO along the flight tracks reveals lowest NO mixing ratios of less than 20 pptv between 2 and 8 km altitude and highest mixing ratios of 0.15-0.2 ppbv above 12 km altitude. Spatial distribution of tropospheric NO above 12 km altitude shows that the
20 sporadically enhanced local mixing ratios (> 0.4 ppbv) occur over the West African continent, which we attribute to episodic lightning events. Measured O₃ shows little variability in mixing ratios at 60-70 ppbv, with slightly decreasing and increasing tendencies towards the boundary layer and stratosphere, respectively. Concurrent measurements of CO, CH₄, OH and HO₂ and H₂O enable calculations of NOPRs along the flight tracks and reveal net ozone destruction at -0.6 to -0.2 ppbv h⁻¹ below 6 km altitude and balance of production and destruction around 7-8 km altitude. We report vertical average NOPRs of 0.2-0.4 ppbv
25 h⁻¹ above 12 km altitude with NOPRs occasionally larger than 0.5 ppbv h⁻¹ over West Africa coincident with enhanced NO. We compare the observational results to simulated data retrieved from the general circulation ECHAM/MESSy Atmospheric Chemistry (EMAC) model. Although the comparison of mean vertical profiles of NO and O₃ indicates good agreement, local deviations between measured and modelled NO are substantial. The vertical tendencies in NOPRs calculated from simulated data largely reproduce those from in situ experimental data. However, the simulation results do not agree well with NOPRs
30 over the West African continent. Both measurements and simulations indicate that ozone formation in the upper tropical troposphere is NO_x-limited.

1 Introduction

The importance of nitrogen oxides ($\text{NO}_x = \text{NO} + \text{NO}_2$) and ozone (O_3) in the photochemistry of the atmosphere is widely
35 acknowledged. Both NO and NO_2 are toxic gases, which degrade surface air quality and regulate the abundance of secondary
tropospheric oxidants (Hosaynali Beygi et al., 2011; Silvern et al., 2018). They are the propagating agents in the formation of
 O_3 and govern photochemical ozone production and removal from the atmosphere (Bozem et al., 2017; Schroeder et al., 2017).
Ozone is a greenhouse gas, negatively affects human health and causes ecosystem damage (Jaffe et al., 2018). It is the primary
precursor of the hydroxyl (OH) radical, which determines the oxidation capacity of the atmosphere and directly controls the
40 concentrations of methane (CH_4), carbon monoxide (CO) and many volatile organic compounds (VOCs) (Thornton et al.,
2002; Bozem et al., 2017). The U.S. Clean Air Act identified ozone as a criteria air pollutant in the 1970s (Jaffe et al., 2018).
Since then and especially in the last decades, increasing effort has been put in the understanding and mitigation of tropospheric
ozone pollution (Fiore et al., 2002; Dentener et al., 2005; West and Fiore, 2005; Lelieveld et al., 2009; Pusede et al., 2015;
Jaffe et al., 2018; Nussbaumer and Cohen, 2020; Tadic et al., 2020). To further resolve the complexity of scientific and policy-
45 related issues of the NO_x - O_3 -VOCs relationship, careful evaluation of model simulations against in situ measurement data is
required (Sillman et al., 1995).

Photochemical ozone formation in the troposphere has been comprehensively described in the literature. Briefly, O_3 is
photochemically formed in chemical reactions between NO_x , $\text{HO}_x (= \text{OH} + \text{HO}_2)$ and VOCs (Crutzen, 1974, Schroeder et al.,
2017). VOCs are here referred to as RH where R stands for an organic residual. The oxidation of CO , CH_4 and VOCs by OH
50 results in the production of HO_2 and peroxy radicals (RO_2).



HO_2 and RO_2 (including CH_3O_2 and further organic peroxy radicals) rapidly oxidize NO to NO_2 , which will yield O_3 in its
55 subsequent photolysis (reaction R6) followed by recombination of atomic ground-state oxygen with molecular oxygen
(reaction R7) (Thornton et al., 2002).



The net effect of reaction R1-R7 on HO_x and NO_x is zero, which is why both act as catalysts in photochemical O_3 production.
Ozone loss is due to photolysis (and subsequent reaction of $\text{O}({}^1\text{D})$ with H_2O) and reactions of O_3 with OH and HO_2 .





Note that the deactivation of $O(^1D)$ to $O(^3P)$ via collisions with N_2 and O_2 will result in the reformation of O_3 (Bozem et al., 2017; Tadic et al., 2020). We express the portion of O_3 that is effectively lost via photolysis by α (see section 2.2). In this study, we neglect chemical loss reactions of O_3 with alkenes, sulphides and halogen radicals. Note that reactions R8-R11 will be referred to as gross ozone loss, while the rate-limiting reactions of NO with HO_2 or RO_2 to produce NO_2 will be referred to as gross ozone production (Zanis et al., 2000a; Thornton et al., 2002). The difference between these two quantities will yield net ozone production, conventionally given in units of $ppbv\ h^{-1}$ (Bozem et al., 2017) or $ppbv\ d^{-1}$ (Tadic et al., 2020).

The dependency of NOPRs on ambient levels of NO_x is highly non-linear (Bozem et al., 2017). Due to the above-mentioned chemistry gross ozone loss will naturally prevail over gross ozone production at low NO_x . Increasing ambient NO_x will result in a linear increase in ozone formation such that the chemical air mass will shift from net destruction to net production in ozone (Bozem et al., 2017; Schroeder et al., 2017). However, at a certain NO mixing ratio, which depends on ambient levels of HO_x and VOCs, adding more NO to the system will result in a saturation in ozone formation and eventually in a decrease in net ozone production towards higher NO levels (Tadic et al., 2020). This is due to the reaction of NO_2 with OH to produce HNO_3 followed by its deposition to the surface.



Reaction R12 will decrease the pool of available HO_x and NO_x radicals from the atmosphere to produce O_3 (Thornton et al., 2002). Ozone formation hence crucially depends on whether NO_x or VOCs are available in excess. These two atmospheric states are commonly referred to as either VOC-limited (if NO_x is available in excess) or as NO_x -limited (if VOCs are available in excess) (Sillman et al., 1995; Sillman et al., 2003; Duncan et al., 2010; Nussbaumer and Cohen, 2020; Tadic et al., 2020).

85 The lifetime of NO_x in the atmosphere varies from a few hours in the planetary boundary layer (PBL) to 1-2 weeks in the upper troposphere/lower stratosphere (UTLS) (Beirle et al., 2010). In the latter, the reaction of NO_2 with OH during daytime and NO_3 formation at nighttime is slowed down due to low ambient pressure and temperature. Transport of NO_x from polluted regions to pristine areas is limited due to the short lifetime of NO_x in the PBL (Reed et al., 2016), which is why NO_x in the troposphere can vary over several orders of magnitude (Miyazaki et al., 2017; Tadic et al., 2020). Whilst measurements performed in remote and pristine regions, such as in the unpolluted South Atlantic marine boundary layer (MBL), have reported NO_x mixing ratios of only a few tens of pptv (Hosaynali Beygi et al., 2011; Fischer et al., 2015), NO_x mixing ratios in urban areas can exceed several tens of ppbv (Lu et al., 2010). Measurements obtained in the polluted MBL around the Arabian Peninsula have shown that NO_x mixing ratios can locally exceed several tens of ppbv even in marine environments in the proximity to strong emission sources such as passing ships or downwind of megacities (Tadic et al., 2020).

95 Ground-level NO_x emissions include fossil fuel combustion, biomass burning and soil emissions (Silvern et al., 2018).
Lightning NO_x (LNO_x), aircraft emissions, and, to a lesser extent, convective uplift of potentially NO_x -rich planetary boundary
air and intrusion of stratospheric air are predominant sources of NO_x in the upper troposphere (Bozem et al., 2017; Miyazaki
et al., 2017). However, estimates of lightning produced NO_x are uncertain (Beirle et al., 2010; Miyazaki et al., 2017) and can
100 have large implications on the photochemistry of the upper troposphere such as over tropical areas where lightning flash rates
are enhanced (Christian et al., 2003; Tost et al. 2007).

A number of previous studies have performed measurements in the region of interest, the troposphere over the Atlantic Ocean
and the West Africa (Lelieveld et al., 2004; Aghedo et al., 2007; Saunois et al., 2009; Real et al., 2010; Bourgeois et al., 2020).
Lelieveld et al. (2004) indicated that positive ozone trends in the marine boundary layer over the Atlantic are likely caused by
an increase in anthropogenic emissions of nitrogen oxides. Aghedo et al. (2007) showed that lightning acts as a major source
105 of tropospheric NO_x , leading to a significant increase in middle and upper tropospheric ozone over the African continent.
Saunois et al. (2009) described results from airborne measurements in the region during the AMMA project. Deploying a two-
dimensional model for further analysis, Saunois et al. determined positive trends in photochemical net ozone production in the
boundary layer over West Africa. There are also results from the ATom airborne mission, which measured vertical profiles of
 O_3 in the troposphere over the Atlantic Ocean (Bourgeois et al., 2020), which we will use to validate the results presented here.
110 Real et al. (2010) investigated downwind O_3 production in pollution plumes in the mid and upper troposphere and determined
mean net ozone production rates of 2.6 ppbv/day over a period of 10 days. However, studies reporting on vertical profiles and
spatial distributions of nitric oxide, ozone and net ozone production rates as part of one coherent measurement project in the
troposphere over the West African continent and the Atlantic Ocean are absent.

In the present study, we characterize the distribution of NO and the role of NO in photochemical processes in the upper tropical
115 troposphere above the Atlantic Ocean and West Africa. The structure of the paper is as follows: we provide methodological,
practical and technical information about the campaign and deployed instrumentation in Sect. 2. In Sect. 3 we present in situ
 NO and O_3 data obtained during the campaign including vertical profiles and spatial distributions. Based on concurrent
measurements of CO , CH_4 , OH and HO_2 , H_2O , the actinic flux density, pressure and temperature net O_3 production rates
(NOPRs) were calculated along the flight tracks. We also provide a comparison of the observational results to simulated data
120 retrieved from the 3-D EMAC model and analyze the dependency of NOPRs on ambient NO . In Sect. 4, we summarize our
results and draw conclusions based on our findings.

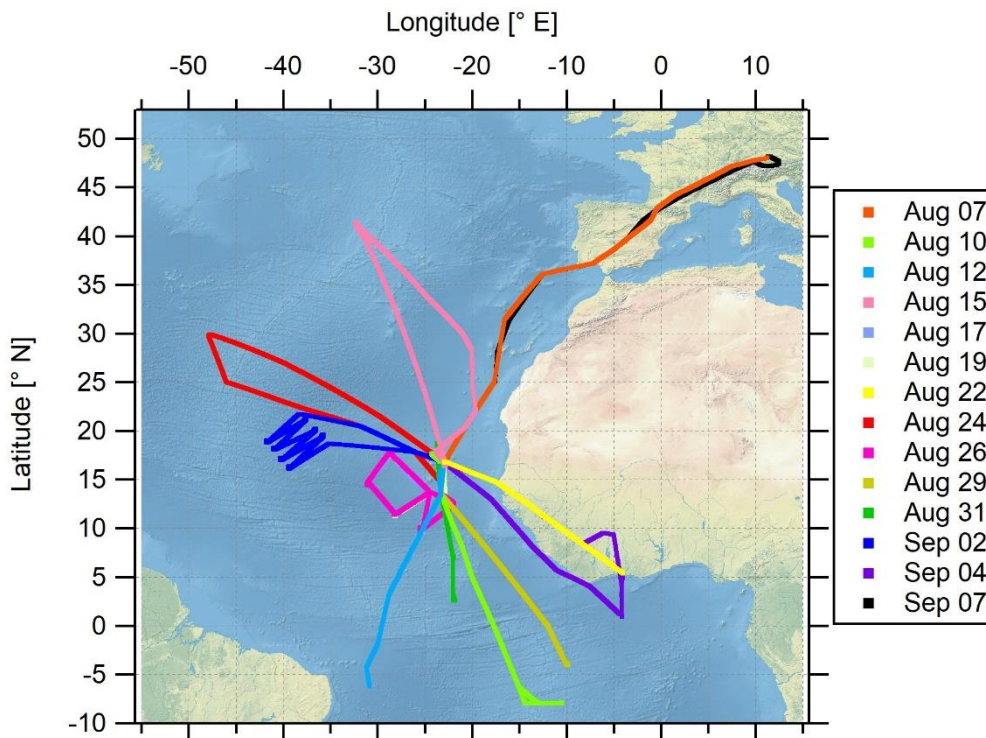
2 Experimental

2.1 CAFE-Africa campaign

The airborne measurement-based CAFE-Africa project took place in August and September 2018 in the tropical troposphere
125 over the Central Atlantic Ocean and the West African continent. Starting from and returning to the international airport on Sal,
Cape Verde (16.75° N , 22.95° W) a total of 14 scientific measurement flights (MFs) was carried out with the German High

Altitude and Long-range research aircraft (HALO). For the analysis of the MFs, we consecutively numerate each MF, starting with MF03 on August 07, 2018 for the ferry flight from Oberpfaffenhofen (Germany, Deutsches Zentrum für Luft- und Raumfahrt) to Sal (Cape Verde Islands) on and ending with MF16 on September 07, 2018 for the back ferry flight from Sal to Oberpfaffenhofen on. The test flights MF01 and MF02 conducted over Germany are not included in this study. MF03-MF16 covered a latitudinal range from 8° S to 48.2° N and a longitudinal range from 47.9° W to 12.5° E and reached maximum flight altitudes of about 15 km. Before landing at the home base airport in Sal, a fixed-altitude leg of 30 min duration at FL150 (~4,600 m altitude) was flown for calibration purposes. Take off (T/O) time of the flights was typically 9 or 10 UTC, except for MF08 with T/O at 4 UTC and landing around 13 UTC and MF11 with T/O at 16 UTC and landing around 1 UTC the next day.

The location of the campaign home base on Sal provided the unique possibility to analyze the impact of the Inter-Tropical convergence zone (ITCZ) on physical and chemical processes in the airspace above the Atlantic Ocean and the West African continent. The ITCZ is a low-pressure region evolving near the equator, which is characterized by deep convection, strong precipitation and frequent lightning (Collier and Hughes, 2011), producing nitrogen oxides, mostly as NO through the Zeldovich reactions from atmospheric N₂ and O₂. The campaign was performed in late summer (August and September) 2018 when the ITCZ had reached its northernmost position at around 5-15° N (Collier and Hughes, 2011) and was henceforth located only a few degrees in latitude to the south of the campaign base at 16.75° N. The flight tracks of the 14 MFs performed during the campaign are shown in Fig. 1. An overview of the corresponding flight dates and objectives of each particular MF is given in the supplementary Table ST1.



145

Figure 1: Spatial orientation of the measurement flight tracks of during CAFE-Africa. Note that MF07 (August 17, 2018), MF08 (August 19, 2018) and MF11 (August 26, 2018) had identical flight tracks.

2.2 Chemiluminescent detection of NO

150

In situ measurements of NO_x on ground-based and mobile platforms are challenging in terms of the demand for high sensitivity and high precision (Tadic et al., 2020). During CAFE-Africa, we deployed a modified commercially available chemiluminescent detector *CLD 790 SR* (ECO Physics Inc., Dürnten, Switzerland) on-board HALO. It is the same instrument that has been used during previous shipborne (Hosaynali Beygi et al., 2011; Tadic et al., 2020) and airborne campaigns (Bozem et al., 2017). The measurement method is based on the gas phase reaction of NO with O_3 , which will partly produce excited-state NO_2^* followed by the spontaneous emission (chemiluminescence) of a photon (Ridley and Howlett, 1967; Ryerson et al., 2000).

155



160

Photons generated through the emissions from excited-state NO_2^* , which are directly proportional to the NO concentration in the sample flow (Ridley and Howlett, 1967), are detected by a photomultiplier tube and converted to an electric pulse. Carrying out the oxidation of NO by O_3 at low-pressure (7-8 mbar) and in a temperature-stabilized (25 °C) main reaction chamber,

minimizes quenching (non-radiative de-excitation of NO_2^* via collisions) (Reed et al., 2016; Tadic et al., 2020). Detector dark noise and artefacts due to the reaction of O_3 with species other than NO (such as alkenes and sulphides) is corrected for by using a pre-chamber setup, as first described by Ridley and Howlett (1967). A residual instrumental background (due to memory effects within the instrument) is corrected for by regularly sampling synthetic zero air (Tadic et al., 2020). During the MFs, we sampled zero air from a tank (17 l composite tank, AVOX) with a Purafil-activated carbon adsorbent installed downstream of the zero-air tank to ensure NO-free zero-air measurements. The residual instrumental background of the NO measurement was calculated at 5 pptv from measurements obtained at nighttime during MF11. As chemiluminescent detection of NO is an indirect measurement method, regular calibrations against a known standard are needed. During the MFs we diluted the secondary NO standard (1.187 ± 0.036 ppmv NO in N_2) at a mass flow of 8.6 sccm in a zero-air flow of 3.44 SLM (standard litre per minute) resulting in NO calibration gas mixing ratios of ~ 3 ppbv. NO calibrations measurements were performed six to eight times during a MF of 9-10 h duration by manually initiating calibration slots consisting of 2 min zero-air measurement, 2 min NO calibration and 2 min zero-air measurement, similar to previous deployments of the instrument (see Tadic et al., 2020).

The limit of detection (LOD) of the NO data was calculated at 9 pptv from the FWHM (full width at half maximum) of a Gauss Fit applied to the distribution of 1 s NO data obtained at nighttime during MF11 (see supplement Figure S1). Analogously we estimate the LOD of the NO data at 1 min time resolution to be 5 pptv from the FWHM of a Gauss Fit applied to the distribution of 1 min NO data obtained at nighttime during MF11. The precision of the NO data was calculated from the average reproducibility of all in-flight calibrations to be 5 % at 1σ . The uncertainty in the used secondary standard mixing ratio was 3 %. The total measurement uncertainty (TMU) of the NO data was estimated at 6 % as the quadratic sum of the precision and the uncertainty of the secondary standard (Tadic et al., 2020).

$$\text{TMU}(\text{NO}) = \sqrt{(5 \%)^2 + (3 \%)^2} \approx 6 \%$$
 (1)

2.3 Further measurements used in this study

O_3 was quantified with a chemiluminescence detector calibrated by a UV photometer (Fast AIRborne Ozone Instrument; Zahn et al., 2012). CO and CH_4 were measured by mid-infrared quantum cascade laser absorption spectroscopy (QCLAS) with TRISTAR, a multi-channel spectrometer (Schiller et al., 2008; Tadic et al., 2017). OH and HO_2 radicals were measured by laser-induced fluorescence with the custom-built HORUS instrument (Marno et al., 2020). Note that both OH and HO_2 data are preliminary. We conservatively estimate the total relative measurement uncertainty of the OH and HO_2 data at 50 %. Spectrally resolved actinic flux density measurements were obtained with two spectro-radiometers (upward- and downward-looking) installed on the top and bottom of the aircraft fuselage, respectively. The particular photolysis frequencies were calculated from the actinic flux density spectra between 280 and 650 nm (Bohn and Lohse, 2017). The uncertainty in the used j -values was estimated to be 13 %. Water vapor mixing ratio and further derived humidity parameters were measured by SHARC (Sophisticated Hygrometer for Atmospheric ResearCh) based on dual path direct absorption measurement by a

tunable diode laser (TDL) system (Krautstrunk and Giez, 2012). The measurement range of SHARC covers the whole
 195 troposphere and lower stratosphere (5-40000 ppmv) with an absolute accuracy of 5 % (+1 ppmv). The BAMAHAS (**BA**sic
HALO Measurement And Sensor System) provided measurements of temperature and pressure (Krautstrunk and Giez, 2012).
 All instruments deployed on the aircraft have been developed to meet the high standards of airborne measurements in terms
 of operability, accuracy and sensitivity. Table 1 lists the used instrumentation with the associated total measurement
 uncertainties. A reference is given regarding the use of each method during previous measurements.

200 **Table 1: List of performed observations with the corresponding total measurement uncertainty (given as a percentage) during
 CAFE-Africa. The last column provides a reference regarding the practical use of the used measurement/instrument.**

Measurement	Technique / method	TMU	reference
NO	chemiluminescence	6 %	Tadic et al., 2020
O ₃	UV photometry / chemiluminescence	2.5 %	Zahn et al., 2012
CO	QCLAS	4.3 %	Tadic et al., 2017
CH ₄	QCLAS	0.3 %	Schiller et al., 2008
OH	LIF	50 %	Marno et al., 2020
HO ₂	LIF with chemical conversion	50 %	Marno et al., 2020
H ₂ O	TDL	5 %	Krautstrunk and Giez, 2012
<i>j</i> (O ¹ D)	spectral radiometer	13 %	Bohn and Lohse, 2017

2.4 ECHAM/MESSy Atmospheric Chemistry (EMAC) model and data analysis

EMAC is a 3-D global general circulation, atmospheric chemistry-climate model, which has been used and described in a
 number of previous studies (Roeckner et al., 2006; Jöckel et al., 2010; Sander et al., 2019; Tadic et al., 2020). Briefly, EMAC
 205 comprises the 5th generation of the **European Center Hamburg** (ECHAM5) circulation model (Roeckner et al., 2006) and the
Modular Earth Submodel System (MESSy) in the version 2.52 (Jöckel et al., 2010). Here we use the model in the T63L47
 resolution with a spatial resolution of roughly 1.8° × 1.8°, 47 vertical levels and one data point every 6 min. The model has
 been weakly nudged towards the ECMWF ERA-Interim data (Jeucke et al., 1996; Berrisford et al., 2009). The chemical
 mechanism (the Mainz Organic Mechanism, MOM) and the photolysis rate calculations used in this work have been presented
 210 in Sander et al. (2019) and in Sander et al. (2014), respectively. The Emissions Database for Global Atmospheric Research
 (EDGARv4.3.2, Crippa et al. 2018) were used for anthropogenic emissions, while biomass burning emissions were from the
 GFAS (Global Fire Assimilation System) database with a daily temporal resolution (Kaiser et al. 2012). Important for this
 work, the NO_x emissions from lightning activity have been estimated using the submodel LNOX (Tost et al., 2007), where the
 parameterization by Grewe et al. (2001) was applied. The global NO_x emissions from lightning were scaled to 6.3 Tg(N)/yr,
 215 following Miyazaki et al. (2014). Tracer and aerosol wet and dry deposition were estimated following Tost et al. (2006) and
 Kerkweg et al. (2006), respectively. The NO_x soil biogenic emission flux is calculated based on a semi-empirical emission
 algorithm implementation by Yienger and Levy II (1995; Kerkweg et al., 2006). For the current study we use EMAC
 simulations of NO, O₃, OH, HO₂, CH₃O₂, specific humidity, *j*(O¹D), temperature and pressure spatially interpolated to the
 flight tracks (latitude, longitude and altitude). Based on the simulations we perform calculations of α and NOPRs along the

220 flight tracks (see section 2.5). To synchronize the time stamp of the model data (6 min) with the measurement data (1 min), we have calculated a running mean of the measurement data within ± 2 min around the simulated data point along the measurement flight tracks such that every sixth measurement data point (if available) was neglected.

2.5 Calculation of net ozone production rates (NOPRs)

225 Calculation of NOPRs utilizes the chemical reactions related to ozone formation described in the introduction. EMAC model calculations show that during CAFE-Africa CH_3O_2 represents on average 80 % of the sum of all organic peroxy radicals with respect to ozone formation at typical flight altitudes of 200 hPa (and even up to 90 % at lower altitudes). Model calculations further show that the sum of HO_2 and CH_3O_2 represents on average 95 % of the sum of HO_2 and all organic peroxy radicals (RO_2) yielding that the ratio $(\text{HO}_2 + \text{CH}_3\text{O}_2)/(\text{HO}_2 + \text{RO}_2)$ is practically one. In analogy to Tadic et al. (2017), we estimated RO_2 as the sum of all organic peroxy radicals with less than four carbon atoms. See supplementary Table ST2 for an overview of
 230 the used organic peroxy radicals. Therewith we calculate photochemical gross production of O_3 by the rate-limiting reaction of NO with HO_2 and CH_3O_2 (Thornton et al., 2002; Bozem et al., 2017).

$$P(\text{O}_3) = [\text{NO}] \cdot (k_{\text{NO}+\text{HO}_2}[\text{HO}_2] + k_{\text{NO}+\text{CH}_3\text{O}_2}[\text{CH}_3\text{O}_2]). \quad (2)$$

The IUPAC Task Group on Atmospheric Chemical Kinetic Data Evaluation (Atkinson et al. 2004; Atkinson et al., 2006) provides rate coefficients used in this study. Note that other studies use $P(\text{O}_3)_{\text{gross}}$ as an acronym for $P(\text{O}_3)$ in Eq. 2. The
 235 photochemical lifetimes of both HO_2 and CH_3O_2 are similar with respect to self-reactions yielding hydrogen peroxide and methyl hydroperoxide and reactions with NO and HO_x (Bozem et al., 2017). We further assume photostationary steady state (PSS) for the probed air masses. As the typical time to acquire PSS during CAFE-Africa varied between 40 s at 2 km altitude and about 70-80 s at 15 km altitude (Mannschreck et al., 2004; Tadic et al., 2020), we can calculate the concentration of CH_3O_2 by the equation derived by Bozem et al. (2017).

$$240 \quad [\text{CH}_3\text{O}_2] = \frac{k_{\text{OH}+\text{CH}_4}[\text{CH}_4]}{k_{\text{OH}+\text{CO}}[\text{CO}]} \cdot [\text{HO}_2] \quad (3)$$

Note that the reaction of CO with OH represents the dominant term in HO_2 production during CAFE-Africa. Assuming mixing ratios of 500 ppbv and 100 pptv for H_2 and HCHO, respectively, we find that HO_2 production rate from the reaction of OH with CO is on average 5 times greater than the sum of the HO_2 production rates from photolysis of HCHO and the reactions of HCHO and H_2 with OH during CAFE-Africa. Note that the assumed mixing ratio of 100 pptv represents a rather
 245 conservative upper estimate for HCHO in the upper troposphere. As mentioned above, ozone loss due to photolysis (and subsequent reaction of $\text{O}(^1\text{D})$ with H_2O) will only partly lead to a net loss effect as most $\text{O}(^1\text{D})$ will deactivate via collisions with air molecules, mostly N_2 and O_2 , to $\text{O}(^3\text{P})$ and reform O_3 in the subsequent reaction with O_2 . The share of O_3 photolysis that will eventually lead to a net loss in O_3 , can be calculated using Eq. 4 (Bozem et al., 2017; Tadic et al., 2020).

$$\alpha = \frac{k_{\text{O}(^1\text{D})+\text{H}_2\text{O}}[\text{H}_2\text{O}]}{k_{\text{O}(^1\text{D})+\text{H}_2\text{O}}[\text{H}_2\text{O}] + k_{\text{O}(^1\text{D})+\text{N}_2}[\text{N}_2] + k_{\text{O}(^1\text{D})+\text{O}_2}[\text{O}_2]} \quad (4)$$

250 In the troposphere, α ranges from about 15 % in the PBL to 1 % in the upper troposphere, where absolute humidity is very low (Bozem et al., 2017). Further loss processes of O_3 (reactions with alkenes, sulphides and halogen radicals) are considered small and are therefore neglected in this study. Equation 5 then gives gross loss of ozone.

$$L(O_3) = [O_3] \cdot (\alpha \cdot j(O^1D) + k_{OH+O_3}[OH] + k_{HO_2+O_3}[HO_2]) \quad (5)$$

$j(O^1D)$ expresses the photolysis frequency of ozone to $O(^1D)$. The NOPR is given as the difference of the gross ozone
255 production rate (Eq. 2) and the gross ozone loss rate (Eq. 5) (Lin et al., 1988, Cantrell et al., 2003).

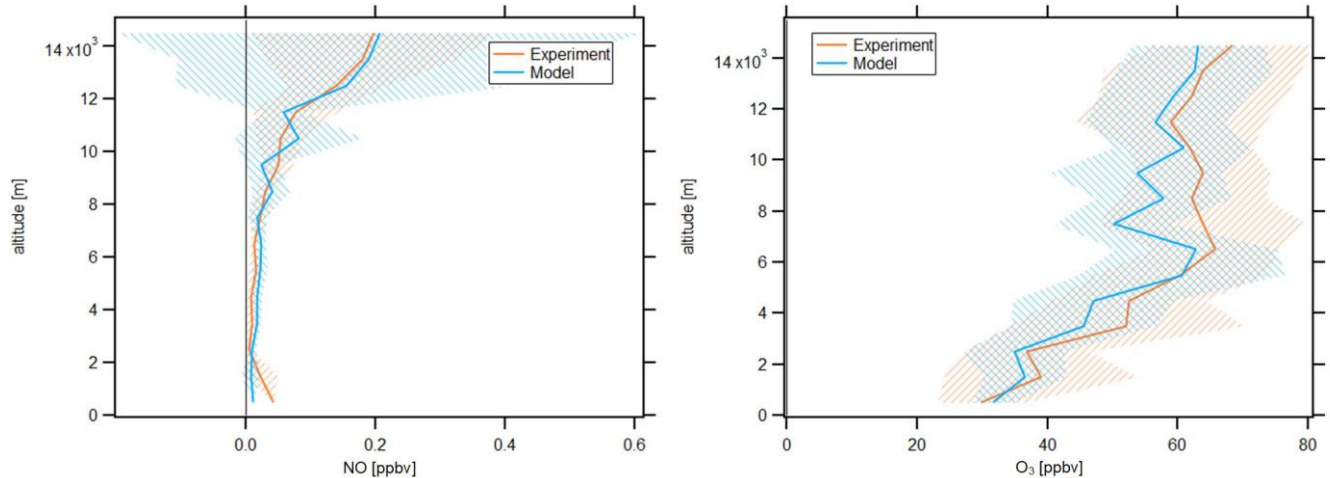
$$\begin{aligned} \text{NOPR} &= P(O_3) - L(O_3) = \\ &[NO] \cdot (k_{NO+HO_2}[HO_2] + k_{NO+CH_3O_2}[CH_3O_2]) - [O_3] \cdot (\alpha \cdot j(O^1D) + k_{OH+O_3}[OH] + k_{HO_2+O_3}[HO_2]) \end{aligned} \quad (6)$$

Note that other studies use $P(O_3)_{\text{net}}$ as an acronym for NOPR in Eq. 6.

3 Results

260 3.1 Vertical profiles of NO and O_3 in the tropical troposphere

In the following, we will investigate averages of the vertical profiles, which are calculated based on an altitude bin width of 1 km. The profiles are calculated with respect to the centre of the particular bin, e.g. the average at 3.5 km includes all data points obtained at or above 3 km altitude and below 4 km altitude. Data are filtered for stratospheric influence by removing all data points for which concurrent O_3 is larger than 100 ppbv; a conservative criterion which has been discussed by Prather et al.
265 (2011). Fig. 2 shows the vertical NO and O_3 profiles obtained during CAFE-Africa. The orange and blue lines represent vertical average profiles of experimental and model simulated data, respectively. The blue and orange shading in the respective colors represent the ± 1 standard deviation of the vertical averages.



270 **Figure 2: Vertical NO (left) and O_3 profiles (right) of measured and modelled data along the flight tracks during CAFE-Africa. Note the large variability of simulated NO mixing ratios above 10 km. The figures have been filtered for stratospheric measurements by removing data points for which O_3 exceeds 100 ppbv.**

The vertical profile of measured NO data shows lowest NO mixing ratios of less than 20 pptv observed between 2 and 8 km altitude, which reflect the absence of emission and transport sources at these altitudes. Highest NO mixing ratios of 0.15-0.2 ppbv are observed above 12 km altitude and reflect the increasing amount of lightning-produced NO_x, and to a lesser extent influence of relatively NO_x-rich stratospheric air. Below 2 km altitude, the vertical profile shows a weak increase of NO, which reproduces the low amount of anthropogenic sources in the investigated MBL and PBL in the proximity to the Cape Verde Islands. This suggests that the contribution of local convective uplift of PBL air to the increased NO_x above 12 km altitude is negligible.

The vertical average profile of simulated NO data is in good agreement with the vertical profile of measured NO data, which is also indicated by the median NO(model)/NO(measurement) ratio throughout the whole campaign at 0.97. Although the vertical profiles are in overall agreement, the variability when comparing single measurement and simulation data points is substantial, as indicated by the large variability of simulated NO data above 10 km altitude. The 25th percentile, 75th percentile and average of the NO(model)/NO(measurement) ratio throughout the whole campaign are 0.25, 2.2 and 2.27, respectively, which illustrate the significant spread among measurement and model data in a comparison of individual data points. The minimum and maximum mixing ratios of modelled NO are zero and 2.13 ppbv, respectively. The minimum and maximum mixing ratios of observed NO are zero and 0.95 ppbv, respectively.

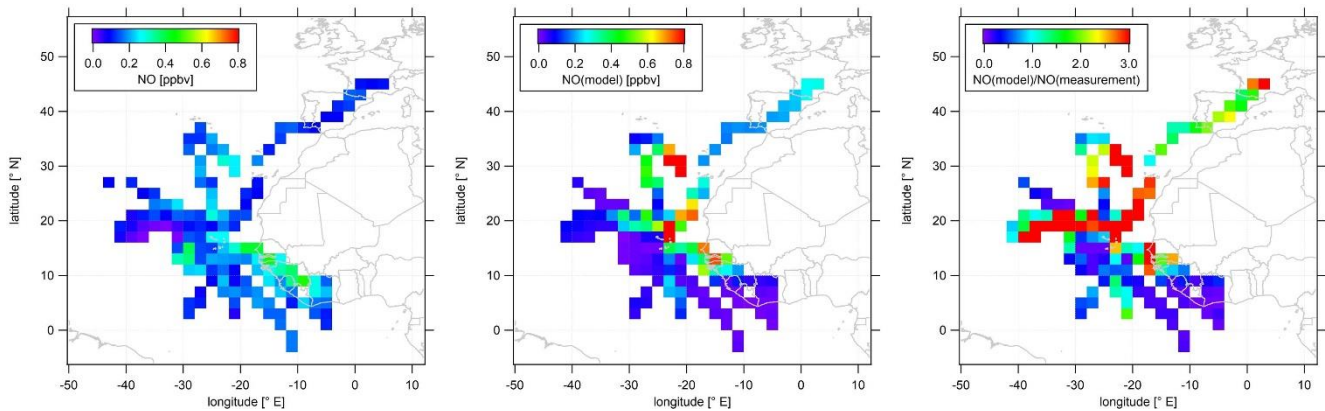
The average vertical profile of measured O₃ shows lowest mixing ratios of 30-40 ppbv below 3 km altitude and a steady increase in O₃ at about 5-10 ppbv per km altitude to mixing ratios of 60-65 ppbv at 6 km. Above this altitude, O₃ is relatively constant (60-65 ppbv) until it further increases above 12 km altitude, simultaneous with the increase in NO.

Although simulated O₃ slightly underestimates the measurement data throughout the troposphere, we find that the vertical profiles of simulated and measured O₃ data are in again in good agreement. EMAC O₃ data match lowest mixing ratios of 30-40 ppbv observed below altitudes of 3 km as well as the vertical gradient in O₃ mixing ratios between 3 and 6 km with mixing ratios of 60 ppbv at 6 km altitude. Above 6 km altitude, both the vertically constant O₃ mixing ratio as well as the further increase in O₃ above 12 km altitude deduced from the measurements are well reproduced by the model. Except for lowest altitudes (< 1 km), it seems that simulated O₃ mixing ratios slightly underestimate the measurement data. This is confirmed by the median and average O₃(model)/O₃(measurement) ratio throughout the campaign at 0.97 and 0.98, respectively, confirming the general agreement between measurements and simulations, as well as the slight underestimation by the latter. The 25th percentile and 75th percentile of the O₃(model)/O₃(measurement) ratio are 0.85 and 1.11, respectively, and indicate that the spread among single data points when comparing measurement and model for O₃ is less than for NO.

O₃ profiles observed in this study are in good agreement with results from the ATom mission (Bourgeois et al., 2020). For the June-August season, Bourgeois et al. show that in the tropical troposphere O₃ increased with altitude to 50 ppbv at 5-6 km whereas above 9 km O₃ varied from 40 to 80 ppbv, supporting the results presented here (see Figures 9 and 10 in Bourgeois et al., 2020).

3.2 Spatial distribution of NO and O₃ in the upper tropical troposphere

305 As most of the measurement time (> 60 %) of the CAFE-Africa campaign was dedicated to upper tropospheric measurements above 12 km altitude and as both NO and O₃ show highest mean mixing ratios above 12 km altitude, we characterize the spatial distribution of NO and O₃ above that altitude in the following. Data above 12 km altitude have been aggregated and averaged over a spatial 2° × 2° grid. We again remove stratospheric measurement data by only considering those for which O₃ was below 100 ppbv. Note that this does not necessarily exclude influence of mixing with air of stratospheric origin. Figure 3
310 shows the color-coded spatial NO distributions based on the measured data (left plot) and simulated data (middle plot). The right plot shows the tropospheric average spatial distribution of the point-by-point NO(model)/NO(measurement) ratio above 12 km. Note that the color scales presented in the following emphasize the most relevant features of the spatial distribution. Thus a few single data points might exceed the given color range, such as in the case of simulated NO (Figure 3, middle plot) with single maximum NO mixing ratios of > 1 ppbv.



315

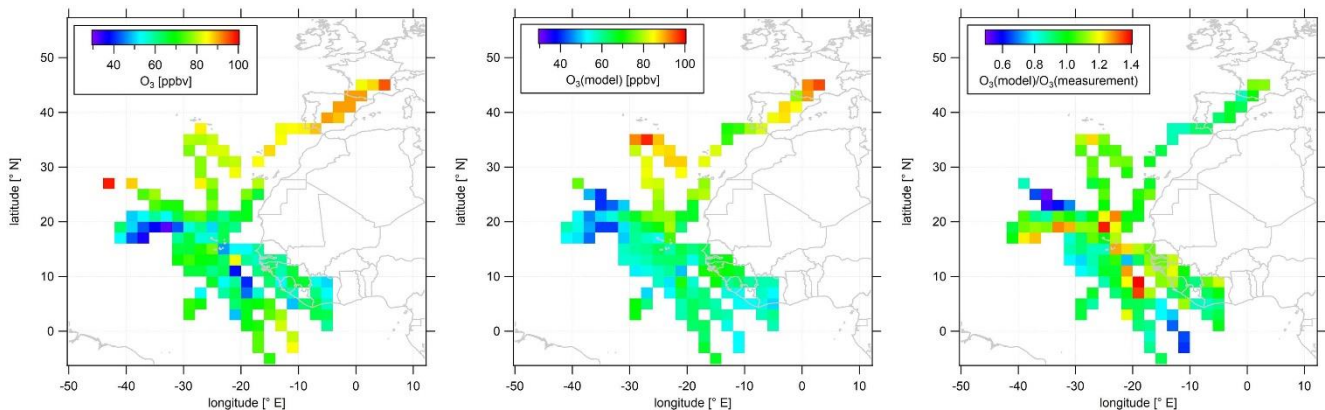
Figure 3: Color-coded spatial, tropospheric NO distributions above 12 km during CAFE-Africa. The left and middle graphs show the measured and simulated NO, respectively. The right graph shows the spatial distribution of the NO(model)/NO(measurement) ratio. The figures have been filtered for stratospheric measurements by removing data points for which O₃ exceeds 100 ppbv.

The spatial distribution of NO from the measurement data shows that NO in the upper tropical troposphere above West Africa and the Atlantic Ocean is generally 0.1-0.2 ppbv. The range in mixing ratios includes lowest NO of less than 20 pptv observed
320 between -30 to -40° E and 16 to 20° N close to a deep convective system without lightning to mixing ratios of 0.1-0.2 ppbv over wide areas over the Atlantic Ocean to (more than) 0.4 ppbv over the West African continent. Although deep convective systems over oceanic regions rarely evolve lightning (Zipser, 1994), we encountered large amounts of NO close to a marine cumulonimbus cloud system with potential lightning activity resulting in more than 0.3 ppbv NO at -28 to -32° E and at 12
325 to 16° N. The coincidence of the ITCZ (5 to 15° N during August and September) and enhancements in upper tropospheric NO above West Africa underlines the substantial influence of the seasonal migration of the ITCZ and its impact on lightning and nitrogen oxides in the upper tropical troposphere (Zipser, 1994; Xu and Zipser, 2012). The data also suggest a longitudinal increase in NO from about 0.1 ppbv observed at -40° E westbound to 0.4 ppbv above the West African continent. Note that we observe a slight decrease in upper tropospheric NO over the Ivory Coast and partly also over Guinea compared to upper

330 tropospheric NO over Senegal, although the lightning flash rate over the Ivory Coast and Guinea is reported to be a factor of about 3 larger than that over Senegal (Collier and Hughes, 2011). A linear fit applied to the longitudinal average profile of all NO data weighted by the standard deviation and collected in the troposphere above 12 km altitude between -42° E and -8° E reveals an increase in average NO of 4-5 pptv per degree longitude (see supplement Figure S2).

Although the comparison of the vertical profiles of measured and simulated NO suggests generally good correspondence
335 between measurements and model simulations, the agreement with respect to the spatial NO distributions in the upper troposphere is much less satisfactory. The EMAC model does not reproduce the large NO enhancements in the area of the ITCZ, as shown in the latitudinal profile of measured and simulated tropospheric NO data above 12 km in Figure S3 in the supplement. On contrary the model tends to underestimate the observations south of 10° N. Interestingly, this holds also for observations above the West African continent (except for the airspace over Senegal around 12 to 14° N) where simulated NO
340 mixing ratios are highest. This general underestimation of the measurements by the model over large parts of West Africa extends to large parts of the Atlantic Ocean between 5 to 15° N. On the other hand, further north the model tends to overestimate the measurements across large areas north of 16° N and west of -20° E with spatially averaged mixing ratios that exceed 1 ppbv. However, reasonable agreement between measurements and numerical results is observed towards and over Southern Europe.

345 Figure 4 shows color-coded spatial O_3 distributions based on observations (left plot) and simulated data (middle plot). The right plot of Figure 4 shows the average tropospheric distribution of the point-by-point $O_3(\text{model})/O_3(\text{measurement})$ ratio. In analogy to supplement Figure S3, supplement Figure S4 shows latitudinal profiles of measured and simulated O_3 mixing ratios obtained above 12 km in the troposphere.



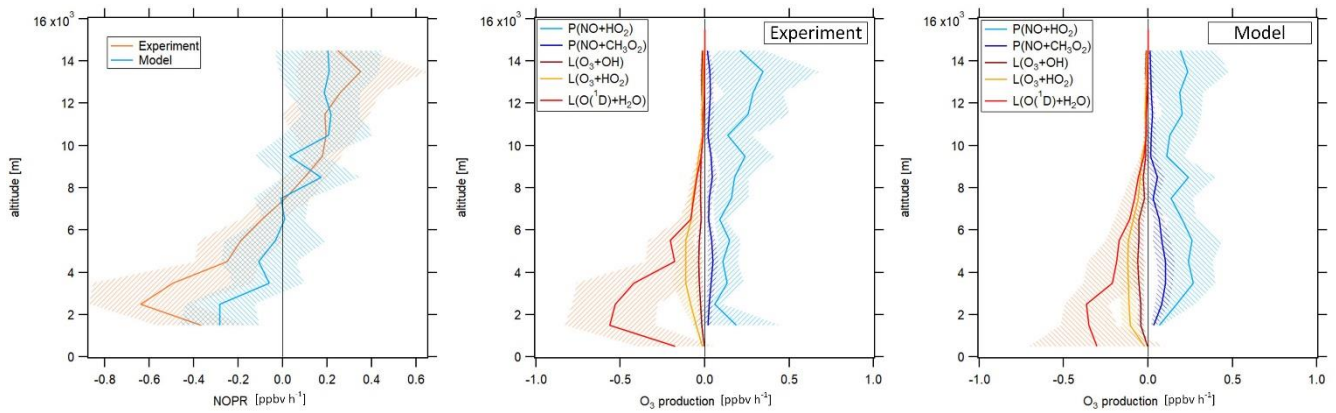
350 **Figure 4: Color-coded spatial, tropospheric O_3 distributions above 12 km during CAFE-Africa. The left and middle graphs show the spatial distribution of measured and simulated O_3 , respectively. The right graph shows the spatial distribution of the $O_3(\text{model})/O_3(\text{measurement})$ ratio. The figures have been filtered for stratospheric measurements by removing data points for which O_3 exceeds 100 ppbv.**

355 Measured O₃ shows a rather uniform distribution in the upper troposphere above the Atlantic Ocean and West African continent. The observed mixing ratios range from less than 40 ppbv between -30 to -40° E and 16 to 20° N, areas where NO is likewise decreased, compared to other regions with more than 80 ppbv towards and over Southern Europe, which partly reflects the increasing stratospheric impact above 12 km altitude. Over the West African continent, we observed average O₃ at 50-70 ppbv, which is in approximate agreement with previous studies (Galanter et al., 2000). Note that measured O₃ mixing ratios over the African continent are not significantly different from O₃ mixing ratios over adjacent oceanic areas.

360 In general, the simulated O₃ reproduces the observed absolute O₃ mixing ratios in the upper tropical troposphere, as well as regional tendencies. It is of note that, although the model underestimates NO over the tropical continental area of Africa, O₃ is reproduced remarkably well. Nevertheless, the model is not able to reproduce local O₃ variations such as at -20° E and 10° N or at -10° E and 0° N. Moreover, simulated O₃ seems to be rather uniformly distributed throughout the whole ITCZ region. The right panel of Figure 4 further illustrates that the majority of the simulated data points deviate by less than 10-15 % from the observational data and that larger deviations between model simulations and measurement are mainly restricted to situations when the measurements show either the lowest or highest mixing ratios, not reproduced by the simulations. The overall spatial agreement between O₃ observation and O₃ simulation is also demonstrated in the latitudinal profile given in supplement Figure S4. Furthermore, supplementary Figures S5 and S6 show 2-D latitudinal/altitudinal distributions of measured, tropospheric NO and O₃, respectively.

370 **3.3 Net ozone production rates in the tropical troposphere**

In the following, NOPRs are calculated based on Eq. 6 and analyzed both vertically and spatially. The left graph of Figure 5 shows the vertical profile of NOPRs derived from measured and simulated data in orange and blue (± 1 standard deviation of the corresponding vertical average), respectively. The middle and right graph show the vertical average profiles of the components of gross ozone loss and gross ozone production derived from experimental in situ data and simulated data, respectively. We provide a vertical profile of α calculated based on Eq. 4, for which we obtain good agreement between measurements and simulations, for which we refer to the left graph of Figure S7 in the supplement. Supplementary Figure S7 also provides a comparison of vertical profiles of measured and simulated H₂O mixing ratios. The vertical profiles are calculated based on an altitudinal bin width of 1 km and are filtered for stratospheric influence by removing data points for which O₃ is higher than 100 ppbv. Supplement Figure S8 presents latitudinal profiles of NOPRs above 12 km altitude in the troposphere derived from measured and simulated data. A spatial distribution of OH and HO₂ (derived from both measured and simulated data) is given in the supplement Figure S9.



385 **Figure 5: Vertical profile of tropospheric NOPRs calculated based on Eq. 6 during CAFE-Africa (left graph). The orange and blue lines represent NOPR calculations based on measured and simulated data, respectively. The middle and right graphs show the components of net ozone production in Eq. 6 derived from experimental data (middle graph) and simulated data (right graph). The figures have been filtered for stratospheric measurements by removing data points for which O_3 exceeds 100 ppbv**

During CAFE-Africa NOPRs derived from in situ measurements varied between -1 ppbv h^{-1} to about 0.6 ppbv h^{-1} within ± 1 standard deviation of the vertical average. We found net ozone destruction for all altitudes below 7-8 km with a minimum of (-0.6 ± 0.2) ppbv h^{-1} between 2 and 3 km. A general increase of NOPRs with altitude results in net ozone production of 0.2 -
 390 0.4 ppbv h^{-1} above 9 km altitude with a maximum of (0.4 ± 0.3) ppbv h^{-1} between 13 and 14 km altitude. The large standard deviation associated with the vertical profile at 13-14 km altitude reflects the large variation in NOPRs along the flight tracks. The vertical NOPR profile derived from in situ data further shows a rather smooth transition from net ozone destruction to net ozone production between 7-8 km altitude, which is in good agreement with the value estimated by Bozem et al. (2017) for the tropical troposphere over the South American rainforest at latitudes of 5 to 10° N. The negative net ozone tendencies
 395 observed between 3 and 5 km altitude for the tropical troposphere stand in opposition to positive net ozone tendencies of about 0.1 ppbv h^{-1} (Zanis et al., 2000a) and balance in net ozone tendencies (NOPR = 0) (HOOVER campaign over Europe; Bozem et al., 2017) deduced from previous measurements at similar altitudes at mid-latitudes.

In general, the vertical tendencies in NOPRs derived from the observations are well reproduced by the NOPR calculation based on simulated data. However, the model calculations indicate a minimum in net ozone destruction at (-0.3 ± 0.2) ppbv h^{-1}
 400 between 1 to 3 km, which represents about half of that derived from the in situ measurements for these altitudes. This underestimation of the measurement by the model is directly related to an underestimation of simulated humidity and $j(O^1D)$, which are both underestimated by EMAC by about 15-20 % below 4 km altitude (see the right graph of supplement Figure S7 for a comparison of the vertical profiles of measured and simulated $j(O^1D)$). The model reports net ozone production of 0.2 ppbv h^{-1} above 8 km (except between 9 and 10 km altitude) and also suggests that the transition from net destruction to net
 405 production occurs between 6 and 8 km altitude, which again agrees with the measurement-based calculation. Nevertheless, the atmospheric variability of the (simulation-based) average NOPR profile reveals that transition from net ozone destruction to net ozone production occurs within a wider altitudinal range of 4 to 10 km altitude.

The reaction of NO with HO₂ dominates gross ozone production (middle graphic, Figure 5) for NOPRs derived from measured in situ data. Whilst the reaction of NO with CH₃O₂ contributes about 0.03 ppbv h⁻¹ to gross ozone production throughout the whole troposphere, the vertical average of the ozone production rate from the reaction of NO with HO₂ yields 0.1 ppbv h⁻¹ at the lowest altitudes with a linear increase ($r^2 \approx 0.6$) to about 0.3 ppbv h⁻¹ at 14-15 km altitude. From our observations it follows that the ozone production rate due to the reaction of NO with HO₂ is from a factor of 2-3 (below 3 km altitude) to a factor of 10 (above 12 km altitude) stronger than gross ozone production due to the reaction of NO with CH₃O₂. For the measurement-based estimate, photolysis of ozone dominates gross ozone loss below 6 km altitude. Between 1 and 2 km, it is largest in absolute values at -0.8 ppbv h⁻¹, where it contributes to about 80 % of total gross ozone loss. With increasing altitude, the gross ozone loss rate due to photolysis sharply decreases in absolute value to less than -0.05 ppbv h⁻¹ above 8 km altitude. Between 6 and 10 km altitude, (total) gross ozone loss is of the order of -0.15 ppbv h⁻¹, mainly due to photolysis of O₃ while reaction of HO₂ with O₃ (-0.05 ppbv h⁻¹) and the reaction of OH with O₃ (-0.03 ppbv h⁻¹) are significantly smaller in absolute values. Above 10 km, gross ozone loss rate decreases to -0.03 to -0.05 ppbv h⁻¹. This is mainly due to a diminishing ozone loss via photolysis and reaction with H₂O at low humidity, leaving ozone loss by the reaction of O₃ with OH and HO₂ at -0.01 to 0.02 ppbv h⁻¹ as major loss processes. Ozone loss rates observed above 10 km during CAFE-Africa have only little impact on NOPRs as they balance only about 10-20 % of the absolute value of concurrent gross ozone production rates at these altitudes.

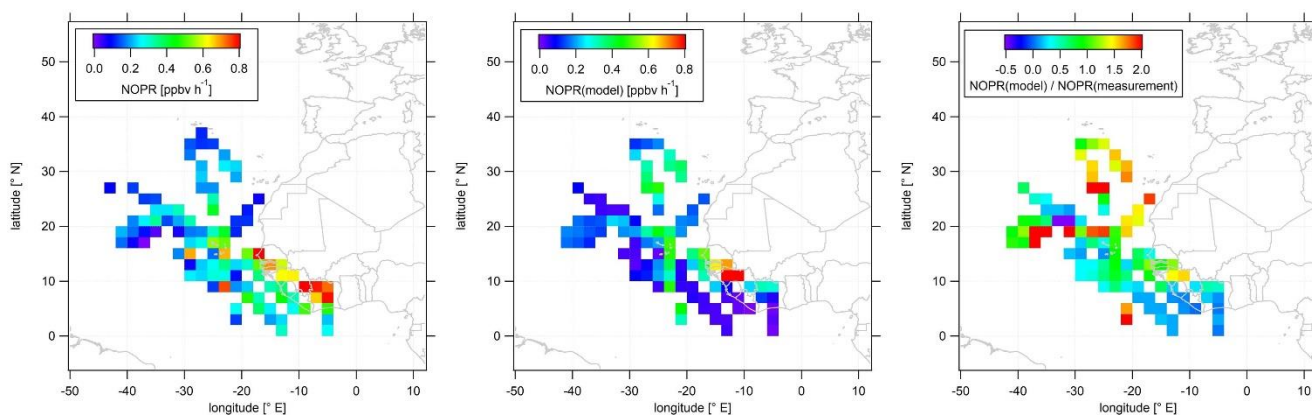
The model generally reproduces the NOPR tendencies in gross production and loss as shown above, yielding net ozone destruction at a rate of -0.1 to -0.3 ppbv h⁻¹ below 4 km altitude, which is significantly lower in absolute values than the measurement based calculation. This is due to a combination of a weaker loss term due to photolysis and of a larger production term due to the reaction of NO with HO₂ and CH₃O₂ represented in the model. The contribution of the reaction of NO with HO₂ represents a vertically constant value of about 0.2-0.3 ppbv h⁻¹ with and a slightly larger production rate from the reaction of NO with CH₃O₂ at 0.05 to 0.1 ppbv h⁻¹ than inferred from the measurements. Above 10 km altitude, EMAC reproduces the relative and absolute tendencies of the particular gross ozone loss rates remarkably well.

Our results are comparable to a previous study on NOPRs derived from in situ airborne observations at similar latitudes over the rainforest in South America (Bozem et al., 2017). Bozem et al. (2017) report net ozone destruction of -0.2 to -0.6 ppbv h⁻¹ between 2 to 4 km and net ozone production between 7 and 9 km altitude with the transition from net ozone destruction to net ozone production occurring at 7 km, similar to our results. Below 6 km altitude gross ozone loss is dominated by photolysis in both studies (Bozem et al., 2017). Bozem et al. (2017) found net ozone production in the continental PBL layer. In this study O₃ destruction prevails, most likely due to the absence of large emission sources in the proximity of the Cape Verde Islands. In the marine boundary layer both studies tend towards net ozone destruction (Bozem et al., 2017).

Our results add to the understanding of photochemical net ozone production in the upper troposphere of the region. Using a photochemical trajectory model initiated by in situ measurements, Real et al. (2010) derived photochemical net ozone production rates of 2.6 ppbv/day over a period of 10 days downwind of West Africa. Our study supports the findings by Real et al. (2010) by underlining that photochemical ozone production in the upper troposphere over the tropics is positive at about

0.2-0.4 ppbv h⁻¹, which supports the concept of significant photochemical ozone production in the upper troposphere of the region. Note that during CAFE-Africa, measurements at low altitudes were generally performed over the Atlantic Ocean. Hence, we cannot compare to previous results from Saunio et al. (2009) reporting ozone production ranging from 0.25 to 0.75 ppbv h⁻¹ in the continental boundary layer over West Africa.

445 In the following, we investigate the spatial distribution of NOPRs derived from measured and simulated data. Figure 6 shows the color-coded spatial, tropospheric distribution of upper tropospheric (> 12 km altitude) NOPRs calculated from observations (left plot) and model simulated data (middle plot). The right plot shows the spatial, average tropospheric distribution of the point-by-point NOPR(model)/NOPR(measurement) ratio. Note that a few single data points exceed the given color scales. Also note that NOPR calculations based on observational data are restricted to periods of simultaneous availability of a number
450 measured species and parameters so that data gaps will be more likely than for spatial distributions of in situ NO or O₃.



455 **Figure 6: Color-coded spatial, tropospheric distributions of calculated NOPRs above 12 km during CAFE-Africa. The left and middle graphs show the spatial distribution of measured and simulated O₃, respectively. The right graph shows the spatial distribution of the NOPR(model)/NOPR(measurement) ratio. The figures have been filtered for stratospheric measurements by removing data points for which O₃ exceeds 100 ppbv.**

The spatial distribution of NOPRs calculated based on measured data shows the already discussed, generally positive net ozone production tendencies in the upper tropical troposphere, but with distinct, characteristic regional features. While NOPRs are generally of the order of (0.2 ± 0.1) ppbv h⁻¹ north of 16° N and west of -20° E, spatially averaged NOPRs in the area of the ITCZ are ~0.4 ppbv h⁻¹ at several locations. Largest spatially averaged NOPRs based on the observations (> 0.8 ppbv h⁻¹) are
460 found over tropical West Africa, mirroring strong NO enhancements (see Figure 3). Nevertheless, the highest NOPR values are inferred over the Ivory Coast although NO is lower than over Guinea or over Senegal, where the NOPR calculation yields comparable, but slightly smaller values. Over the Ivory Coast ozone formation is mainly driven by large HO₂ mixing ratios of up to 15-20 pptv (see supplement Figure S9 for spatial distributions of in situ measured and simulated OH and HO₂ data). Similar as for NO, the spatial distribution further suggest a longitudinal increase of NOPRs towards the West African coast

465 reflecting the general absence of LNO_x over oceanic areas and increased lightning flash rates over the tropical parts of West and Central Africa (Williams and Satori, 2004; Collier and Hughes, 2011).

The spatial distribution of NOPRs calculated based on simulated data largely follows the spatial distribution of simulated NO. Although the model indicates lowest NOPRs of less than 0.2 ppbv h^{-1} over most oceanic area, NOPRs derived from simulated data exhibit values of about 0.4 ppbv h^{-1} at several locations between -20 and -30° E , which correlate with enhancements in
470 NO retrieved from EMAC. Over Africa, EMAC yields significant enhancements in NOPRs only between 10 and 14° N over Senegal, where NO is also enhanced.

The strong dependence of ozone formation on ambient NO concentrations for both measurement and model raises the question to which extent ozone formation was NO_x -limited. Figure 7 shows NOPRs calculated based on measured and simulated data in orange and blue, respectively, aggregated to a bin width of 0.025 ppbv of NO on the x -axis. There is only limited data
475 coverage for measured NO above 0.325 ppbv and for simulated NO above 0.15 ppbv . See supplementary Table ST3 for the number of data points in each NO mixing ratio bin.

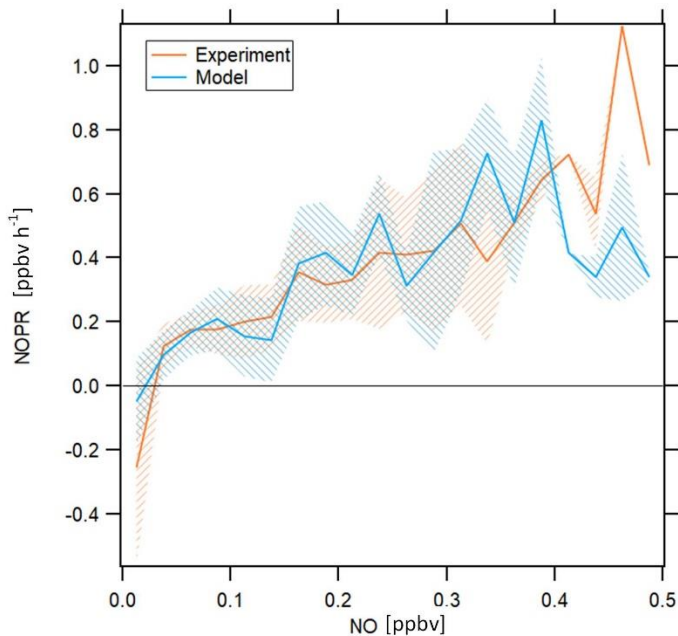


Figure 7: NOPRs derived from measured and simulated data as a function of NO mixing ratios. The orange and blue lines represent average profiles calculated based on measured and simulated data, respectively. The blue and orange shading represent ± 1 standard deviations of the average lines. The profiles have been filtered for stratospheric measurements by removing data points for which O_3 exceeds 100 ppbv .
480

NOPRs derived from both observations and model simulations exhibit similar dependencies on ambient NO mixing ratios. Both measurements and model simulations show net ozone destruction below 30 and 20 pptv, respectively, and a nearly linear increase in NOPRs with increasing ambient NO mixing ratios above this threshold value, with an NOPR increase of 0.1 to

485 0.15 ppbv h⁻¹ per 100 pptv increase in NO. Especially the NO compensation mixing ratio (for which ozone production equals
ozone loss) reproduces results from previous studies remarkably well. Cantrell et al. (2003) report NO compensation mixing
ratios between 10 and 30 pptv over the Pacific, depending on whether modelled or measured HO₂ and RO₂ is used. A study
conducted by Zanis et al. (2000b) for the Swiss Alps also reports balance in ozone production for similar NO compensation
490 increase in NOPR will continue. Note that one possible limitation of this figure arises from the fact that the data aggregated in
the respective NO mixing ratio bins stem from different atmospheric layers and origins, which causes the spiky signature of
the profile for both measurement and model. However, both model simulations and observations indicate that O₃ in the upper
troposphere in the tropics is NO_x-limited.

4 Conclusion

495 We presented in situ observations of NO, O₃ and a number of species involved in photochemical O₃ formation obtained in the
upper tropical troposphere above the Atlantic Ocean and West Africa and compared these experimental results to simulated
data retrieved from the global EMAC chemistry-climate model. Our results corroborate the overall eightfold increase of
lightning flash rates over land compared to oceanic areas, and the associated NO production (Christian et al., 2003), as well as
the notion that tropical Africa is one of the world's lightning hot spots (Williams and Satori, 2004) where large amounts of
500 NO are naturally produced in the process of convection. Observed NO mixing ratios reveal a typical vertical average profile
with lowest NO mixing ratios of less than 20 pptv in the free and middle troposphere and highest mixing ratios of 150-200
pptv above 12 km altitude. We report highest NO (> 0.4 ppbv) in the latitudinal range of the ITCZ (5° N to 15° N) and moreover
over tropical West Africa. While we find overall good agreement when comparing average profiles of observed and EMAC
model simulated NO, large deviations are sometimes found for point-to-point comparisons. The model does not reproduce the
505 largest NO enhancements over West Africa and instead predicts highest NO values above 12 km altitude over large areas of
the North Atlantic, which highlights the importance of an accurate representation of lightning NO in the model. Based on in
situ measurements we found 60-70 ppbv O₃ in the upper tropical troposphere, which is well reproduced by the model. While
the average vertical profile of NOPRs derived from in situ measurements varied vertically between -0.6 ppbv h⁻¹ between 2
and 4 km altitude and 0.2-0.4 ppbv h⁻¹ in the upper tropical troposphere, with a crossover in O₃ formation at around 8 km. A
510 spatial distribution of NOPRs in the upper tropical troposphere created based on experimental in situ data indicates highest
values over the West African continent, which is a result of large NO and HO₂ over the particular regions. Although the model
simulations largely reproduce the observation-based NOPR values, this is at least partly due to compensating effects, e.g. low
NO in the model is partly associated with enhanced HO₂ leading to locally increased NOPRs in the simulations. Overall both
the observations and the model simulations exhibit a nearly linear dependency of NOPRs on ambient NO indicating NO_x-
515 limitation of O₃-formation.

Data availability

Data used in this study are available to all scientists agreeing to the CAFE-Africa data protocol at <https://doi.org/10.5281/zenodo.4442616>.

520 Author contributions

IT, CMN, JL and HF designed the study. IT wrote the manuscript. IT and CMN processed and analyzed the data. IT and UP performed the NO, CO and CH₄ measurements during the campaign. IT processed the NO, CO and CH₄ data. DM, HH, MM and RR performed the OH and HO₂ measurements. BB supervised measurements and processed the actinic flux data. MZ supervised measurements and processed the water vapor data. FO supervised measurements and processed the O₃ data. AP generated model data.

Competing interest

The authors declare that they have no conflict of interest.

Acknowledgements

530 We acknowledge the collaborations with Forschungszentrum Jülich, Karlsruhe Institute of Technology, Heidelberg University, Deutsches Zentrum für Luft- und Raumfahrt and Wuppertal University during the CAFE-Africa campaign. We thank all involved in the CAFE-Africa project for a successful campaign.

Appendix: Acronyms and abbreviations

General

535 CAFE-Africa Chemistry of the Atmosphere: Field Experiment in Africa
HALO High Altitude and Long-range research aircraft

Scientific

CLD Chemiluminescence detector
ECHAM5 Fifth generation European Centre Hamburg general circulation model
EMAC ECHAM/MESSy Atmospheric Chemistry model
540 FAIRO Fast Airborne Ozone Instrument
HORUS Hydroxyl Radical measurement Unit based on fluorescence Spectroscopy instrument
HO_x OH + HO₂
ITCZ Inter-Tropical convergence zone
LIF Laser induced fluorescence
545 MBL Marine boundary layer
MESSy Modular Earth Submodel System
MF Measurement flight
NOPR Net ozone production rate
NO_x NO + NO₂
550 PBL Planetary Boundary Layer
PSS Photostationary steady state
QCLAS Quantum cascade laser absorption spectroscopy
SHARC Sophisticated Hygrometer for Atmospheric ResearCh)
SLM Standard litre per minute

555	TDL	<u>T</u> nable <u>d</u> iode <u>l</u> aser
	TMU	<u>T</u> otal <u>m</u> easurement <u>u</u> ncertainty
	T/O	<u>T</u> ake <u>o</u> ff
	VOC	<u>V</u> olatile <u>o</u> rganic <u>c</u> ompound
	UTC	<u>C</u> oordinated <u>u</u> niversal <u>t</u> ime
560	UTLS	<u>U</u> pper <u>t</u> roposphere/ <u>l</u> ower <u>s</u> tratosphere

References

- Aghedo, A. M., Schultz, M. G., and Rast, S.: The influence of African air pollution on regional and global tropospheric ozone, *Atmos. Chem. Phys.*, **7**, 1193-1212, <https://doi.org/10.5194/acp-7-1193-2007>, 2007.
- Atkinson, R., Baulch, D. L., Cox, R. A., Crowley, J. N., Hampson, R. F., Hynes, R. G., Jenkin, M. E., Rossi, M. J., and Troe, J.: Evaluated kinetic and photochemical data for atmospheric chemistry: volume I gas phase reactions of O_x, HO_x, NO_x and SO_x species, 2004, *Atmos. Chem. Phys.*, **4**, 1461-1738, <https://doi.org/10.5194/acp-4-1461-2004>, 2004.
- Atkinson, R., Baulch, D. L., Cox, R. A., Crowley, J. N., Hampson, R. F., Hynes, R. G., Jenkin, M. E., Rossi, M. J., and Troe, J.: Evaluated kinetic and photochemical data for atmospheric chemistry: volume I gas phase reactions of organic species, *Atmos. Chem. Phys.*, **6**, 3625-4055, <https://doi.org/10.5194/acp-6-3625-2006>, 2006.
- 570 Beirle, S., Huntrieser, H., and Wagner, T.: Direct satellite observations of lightning-produced NO_x, *Atmos. Chem. Phys.*, **10**, 10965-10986, <https://doi.org/10.5194/amt-10-10965-2010>, 2010.
- Berrisford, P., Dee, D. P. K. F., Fielding, K., Fuentes, M., Kallberg, P., Kobayashi, S., and Uppala, S.: The ERA-Interim archive, *ERA report series*, No. 1 ECMWF: Reading, UK, 2009.
- Bohn, B. and Lohse, I.: Calibration and evaluation of CCD spectroradiometers for ground-based and airborne measurements of spectral actinic flux densities, *Atmos. Meas. Tech.*, **10**, 3151–3174, <https://doi.org/10.5194/amt-10-3151-2017>, 2017.
- 585 Bourgeois, I., Peischl, J., Thompson, C. R., Aikin, K. C., Campos, T., Clark, H., Commane, R., Daube, B., Diskin, G. W., Elkins, J. W., Gao, R.-S., Gaudel, A., Hints, E. J., Johnson, B. J., Kivi, R., McKain, K., Moore, F. L., Parrish, D. D., Querel, R., Ray, E., Sánchez, R., Sweeney, C., Tarasick, D. W., Thompson, A. M., Thouret, V., Witte, J. C., Wofsy, S. C., and Ryerson, T. B.: Global-scale distribution of ozone in the remote troposphere from the ATom and HIPPO airborne field missions, *Atmos. Chem. Phys.*, **20**, 10611–10635, <https://doi.org/10.5194/acp-20-10611-2020>, 2020.
- Bozem H., Butler T. M., Lawrence M. G., Harder H., Martinez M., Kubistin D., Lelieveld J., Fischer H.: Chemical processes related to net ozone tendencies in the free troposphere, *Atmos. Chem. Phys.*, **17**, 10565-10582, <https://doi.org/10.5194/acp-17-10565-2017>, 2017.
- Cantrell, C. A., Edwards, G. D., Stephens, S., Mauldin, R. L., Zondlo, M. A., Kosciuch, E., Eisele, F. L., Shetter, R. E., Lefer, B. L., Hall, S., Flocke, F., Weinheimer, A., Fried, A., Apel, E., Kondo, Y., Blake, D. R., Blake, N. J., Simpson, I. J., Bandy, A. R., Thornton, D. C., Heikes, B. G., Singh, H. B., Brune, W. H., Harder, H., Martinez, M., Jacob, D. J., Avery, M. A., Barrick, J. D., Sachse, G. W., Olson, J. R., Crawford, J. H., and Clarke, A. D.: Peroxy radical behavior during the Transport

- and Chemical Evolution over the Pacific (TRACE-P) campaign as measured aboard the NASA P-3B aircraft, *J. Geophys. Res.*, **108**, D20, <https://doi.org/10.1029/2003JD003674>, 2003.
- 590 Christian, H. J., Blakeslee, R. J., Boccippio, D. J., Boeck, W. L., Buechler, D. E., Driscoll, K. T., Goodman, S. J., Hall, J. M., Koshak, W. J., Mach, D. M., and Stewart, M. F.: Global frequency and distribution of lightning as observed from space by the Optical Transient Detector, *J. Geophys. Res.*, **108**, D1, 4005, <https://doi.org/10.1029/2002DJ002347>, 2003.
- Collier, A. B., and Hughes, A. R. W.: A harmonic model for the temporal lightning activity over Africa, *J. Geophys. Res.*, **116**, D05105, <https://doi.org/10.1029/2010JD014455>, 2011.
- 595 Crippa, M., Guizzardi, D., Muntean, M., Schaaf, E., Dentener, F., van Aardenne, J. A., Monni, S., Doering, U., Olivier, J. G. J., Pagliari, V., and Janssens-Maenhout, G.: Gridded emissions of air pollutants for the period 1970–2012 within EDGAR v4.3.2, *Earth Syst. Sci. Data*, **10**, 1987–2013, <https://doi.org/10.5194/essd-10-1987-2018>, <https://www.earth-syst-sci-data.net/10/1987/2018/>, 2018.
- 600 Crutzen, P. J.: Photochemical reactions initiated by and influencing ozone in unpolluted tropospheric air, *Tellus*, **26**, 48–57, <https://doi.org/10.1111/j.2153-3490.1974.tb01951.x>, 1974.
- Dentener, F., Stevenson, D., Cofala, J., Mechler, R., Amann, M., Bergamaschi, P., Raes, F., and Derwent, R.: The impact of air pollutant and methane emission controls on tropospheric ozone and radiative forcing: CTM calculations for the period 1990–2030, *Atmos. Chem. Phys.*, **5**, 1731–1755, <https://doi.org/10.5194/acp-5-1731-2005>, 2005.
- Duncan, B. N., Yoshida, Y., Olson, J. R., Sillman, S., Martin, R. V., Lamsal, L., Hu, Y., Pickering, K. E., Retscher, C., Allen, D. J., Crawford, J. H.: Application of OMI observations to a space-based indicator of NO_x and VOC controls on surface ozone formation, *J. Atmos. Env.*, **44**, 2213–2223, doi:10.1016/j.atmosenv.2010.03.010, 2010.
- 605 Fiore, A. M., Jacob, D. J., Bey, I., Yantosca, R. M., Field, B. D., Fusco, A. C., and Wilkinson, J. G.: Background ozone over the United States in summer: Origin, trend, and contribution to pollution episodes, *J. Geophys. Res.*, **107**, D15, 4275, <https://doi.org/10.1029/2001JD000982>, 2002.
- 610 Galanter, M., Levy, H., Carmichael, G. R.: Impacts of biomass burning on tropospheric CO, NO_x and O₃, *J. Geophys. Res.*, **105**, D5, 6633–6653, <https://doi.org/10.1029/1999JD901113>, 2000.
- Grewe, V., Brunner, D., Dameris, M., Grenfell, J., Hein, R., Shindell, D., and Staehelin, J.: Origin and variability of upper tropospheric nitrogen oxides and ozone at northern mid-latitudes, *Atmos. Environ.*, **35**, 3421–3433, [https://doi.org/10.1016/S1352-2310\(01\)00134-0](https://doi.org/10.1016/S1352-2310(01)00134-0), 2001.

- 615 Hosaynali Beygi, Z., Fischer, H., Harder, H. D., Martinez, M., Sander, R., Williams, J., Brookes, D. M., Monks, P. S., Lelieveld, J.: Oxidation photochemistry in the Southern Atlantic boundary layer: unexpected deviations of photochemical steady state, *Atmos. Chem. Phys.*, **11**, 8497-8513, <https://doi.org/10.5194/acp-11-8497-2011>, 2011
- Jaffe, D. A., Cooper, O. R., Fiore, A. M., Henderson, B. H., Tonnesen, G. S., Russell, A. G., Henze, D. K., Langford, A. O., Lin, M., and Moore, T.: Scientific assessment of background ozone over the US.: Implications for air quality management, *Elem. Sci. Anth.*, **6**, 56, <https://doi.org/10.1526/elementa.309>, 2018.
- 620 Jeucken, A. B. M., Siegmund, P. C., and Heijboer, L. C.: On the potential of assimilating meteorological analyses in a global climate model for the purpose of model validation, *J. Geophys. Res.*, **101**, D12, 16939-16950, <https://doi.org/10.1029/96JD01218>, 1996
- Jöckel, P., Kerkweg A., Pozzer, A., Sander, R., Tost, H., Riede, H., Baumgartner, A., Gromov, S., and Kern, B.: Development of cycle 2 of the Modular Earth Submodel System (MESSy2), *Geosci. Model Dev.*, **3**, 717-752, <https://doi.org/10.5194/gmd-3-717-2010>, 2010.
- 625 Kaiser, J. W., Heil, A., Andreae, M. O., Benedetti, A., Chubarova, N., Jones, L., Morcrette, J.-J., Razinger, M., Schultz, M. G., Suttie, M., and van der Werf, G. R.: Biomass burning emissions estimated with a global fire assimilation system based on observed fire radiative power, *Biogeosciences*, **9**, 527-554, <https://doi.org/10.5194/bg-9-527-2012>, 2012.
- 630 Kerkweg, A., Buchholz, J., Ganzeveld, L., Pozzer, A., Tost, H., and Jöckel, P.: Technical Note: An implementation of the dry removal processes DRY DEPosition and SEDimentation in the Modular Earth Submodel System (MESSy), *Atmos. Chem. Phys.*, **6**, 4617–4632, <https://doi.org/10.5194/acp-6-4617-2006>, 2006.
- Kley, D., Drummond, J. W., McFarland, M., and Liu, S. C.: Tropospheric profiles of NO_x, *J. Geophys. Res.*, **86**, C4, 3153-3161, <https://doi.org/10.1029/JC086iC04p03153>, 1981.
- 635 Krautstrunk, M., Giez, A.: The Transition From FALCON to HALO Era Airborne Atmospheric Research, in: Schumann U. (eds) Atmospheric Physics. Research Topics in Aerospace, *Springer*, Berlin, Heidelberg, https://doi.org/10.1007/978-3-642-30183-4_37, 2012.
- Lelieveld, J., van Aardenne, J., Fischer, H., de Reus, M., Williams, J., and Winkler, P.: Increasing Ozone over the Atlantic Ocean, *Science*, **304**, Issue 5676, 1483-1487, <https://doi.org/10.1126/science.1096777>, 2004.
- 640 Lelieveld, J., Hoor, P., Jöckel, P., Pozzer, A., Hadjinicolaou, P., Cammas, J.-P., and Beirle, S.: Severe ozone air pollution in the Persian Gulf region, *Atmos. Chem. Phys.*, **9**, 1393–1406, <https://doi.org/10.5194/acp-9-1393-2009>, 2009.

- Lin, X., Trainer, M., and Liu, S. C.: On the nonlinearity of the tropospheric ozone production, *J. Geophys. Res.*, **93**, D12, <https://doi.org/10.1029/JD093iD12p15879>, 1988.
- Lu, K., Zhang, Y., Su, H., Brauers, T., Chou, C. C., Hofzumahaus, A., Liu, S. C., Kita, K., Kondo, Y., Shao, M., Wahner, A.,
645 Wang, J., Wang, X., and Zhu, T.: Oxidant ($O_3 + NO_2$) production processes and formation regimes in Beijing, *J. Geophys. Res.*, **115**, D07303, <https://doi.org/10.1029/2009JD012714>, 2010.
- Mannschreck, K., Gilge, S., Plass-Duelmer, C., Fricke, W., and Berresheim, H.: Assessment of the applicability of NO-NO₂-O₃ photostationary state to long-term measurements at the Hohenpeissenberg GAW Station, Germany, *Atmos. Chem. Phys.*, **4**, 1265-1277, <https://doi.org/10.5194/acp-4-1265-2004>, 2004.
- 650 Marno, D., Ernest, C., Hens, K., Javed, U., Klimach, T., Martinez, M., Rudolf, M., Lelieveld, J., and Harder, H.: Calibration of an airborne HO_x instrument using the All Pressure Altitude-based Calibrator for HO_x Experimentation (APACHE), *Atmos. Meas. Tech.*, **13**, 2711-2731, <https://doi.org/10.5194/amt-13-2711-2020>, 2020.
- Miyazaki, K., Eskes, H. J., Sudo, K., and Zhang, C.: Global lightning NO_x production estimated by an assimilation of multiple satellite data sets, *Atmos. Chem. Phys.*, **14**, 3277–3305, <https://doi.org/10.5194/acp-14-3277-2014>, 2014.
- 655 Miyazaki, K., Eskes, H., Sudo, K., Folkert Boersma, K., Bowman, K., and Kanaya, Y.: Decadal changes in global surface NO_x emissions from multi-constituent satellite data assimilation, *Atmos. Chem. Phys.*, **17**, 807-837, <https://doi.org/10.5194/acp-17-807-2017>, 2017.
- Nussbaumer, C. M., and Cohen, R. C.: The role of temperature and NO_x in ozone trends in the Los Angeles Basin, *Environ. Sci. Technol.*, **54**, 15652-15659, <https://doi.org/10.1021/acs.est.0c04910>, 2020.
- 660 Prather, M. J., Zhu, X., Tang, Q., Hsu, J., and Neu, J. L.: An atmospheric chemist in search of the tropopause, *J. Geophys. Res.*, **116**, D04306, <https://doi.org/10.1029/2010JD014939>, 2011.
- Pusede, S. E., Steiner, A., and Cohen, R. C.: Temperature and recent trends in the chemistry of continental surface ozone, *Chem. Rev.*, **115**, 10, 3898-3918, <https://doi.org/10.1021/cr5006815>, 2015.
- Real, E., Orlandi, E., Law, K. S., Fierli, F., Josset, D., Cairo, F., Schlager, H., Borrmann, S., Kunkel, D., Volk, C. M., McQuaid,
665 J. B., Stewart, D. J., Lee, J., Lewis, A. C., Hopkins, J. R., Ravegnani, F., Ulanovski, A., and Liousse, C.: Cross-hemispheric transport of central African biomass burning pollutants: implications for downwind ozone production, *Atmos. Chem. Phys.*, **10**, 3027–3046, <https://doi.org/10.5194/acp-10-3027-2010>, 2010.

- Reed, C., Evans, M. J., Carlo, P. D., Lee, J. D., Carpenter, L. J.: Interferences in photolytic NO₂ measurements: explanation for an apparent missing oxidant?, *Atmos. Chem. Phys.*, **16**, 4707-4724, <https://doi.org/10.5194/acp-16-4707-2016>, 2016.
- 670 Ridley, B. A., and Howlett, L. C.: An instrument for nitric oxide measurements in the stratosphere, *Rev. Sci. Instrum.*, **45**, 6, <https://doi.org/10.1063/1.1686726>, 1974.
- Roeckner, E., Brokopf, R., Esch, M., Giorgetta, M., Hagemann, S., Kornblueh, L., Manzini, E., Schlese, U., and Schulzweida, U.: Sensitivity of Simulated Climate to Horizontal and Vertical Resolution in the ECHAM5 Atmosphere Model, *J. Climate*, **19**, 3771-3791, <https://doi.org/10.1175/JCLI3824.1>, 2006.
- 675 Ryerson, T.B., Williams, E. J., Fehsenfeld, F. C.: An efficient photolysis system for fast-response NO₂ measurements, *J. Geophys. Res.*, **105**, 447-461, <https://doi.org/10.1029/2000JD900389>, 2002.
- Sander, R., Jöckel, P., Kirner, O., Kunert, A. T., Landgraf, J., and Pozzer, A.: The photolysis module JVAL-14, compatible with the MESSy standard, and the JVal PreProcessor (JVPP), *Geosci. Model Dev.*, **7**, 2653–2662, <https://doi.org/10.5194/gmd-7-2653-2014>, 2014.
- 680 Saunio, M., Reeves, C. E., Mari, C. H., Murphy, J. G., Stewart, D. J., Mills, G. P., Oram, D. E., and Purvis, R. M.: Factors controlling the distribution of ozone in the West African lower troposphere during the AMMA (African Monsoon Multidisciplinary Analysis) wet season campaign, *Atmos. Chem. Phys.*, **9**, 6135-6155, <https://doi.org/10.5194/acp-9-6135-2009>, 2009.
- 685 Sander, R., Baumgartner, A., Cabrera-Perez, D., Frank, F., Gromov, S., Groöb, J.-U., Harder, H., Huijnen, V., Jöckel, P., Karydis, V. A., Niemeyer, K. E., Pozzer, A., Riede, H., Schultz, M. G., Taraborrelli, D., and Tauer, S.: The community atmospheric chemistry box model CAABA/MECCA-4.0, *Geosci. Model Dev.*, **12**, 1365-1385, <https://doi.org/10.5194/gmd-12-1365-2019>, 2019.
- Schiller, C. I., Bozem, H., Gurk, C., Parchatka, U., Königstedt, R., Harris, G. W., Lelieveld, J., and Fischer, H.: Applications of quantum cascade lasers for sensitive trace gas measurements of CO, CH₄, N₂O, and HCHO, *Appl. Phys. B*, **92**, 419–430, <https://doi.org/10.1007/s00340-008-3125-0>, 2008.
- 690 Schroeder, J. S., Crawford, J. H., Fried, A., Walega, J., Weinheimer, A., Wisthaler, A., Müller, M., Mikoviny, T., Chen, G., Shook, M., Blake, D. R., and Tonnesen, G. S.: New insights into the column CH₂O/NO₂ ratio as an indicator of near-surface ozone sensitivity, *J. Geophys. Res. Atmos.*, **122**, 8885-8907, <https://doi.org/10.1002/2017JD026781>, 2017.

- 695 Sillman, S., Al-Wali, K., Marsik, F. J., Nowacki, P., Samson, P. J., Rodgers, M. O., Garland, L. J., Martinez, J. E., Stoneking, C., Imhoff, R., Lee, J. H., Newman, L., Weinstein-Lloyd, J., and Aneja, V.: Photochemistry of ozone formation in Atlanta, GA - models and measurements, *Atmos. Environ.*, **29**, 21, 3055-3066., doi:10.1016/1352-2310(95)00217-M, 1995.
- Sillman, S., Vautard, R., Menut, L., and Kley, D.: O₃-NO_x-VOC sensitivity and NO_x-VOC indicators in Paris: Results from models and Atmospheric Pollution Over the Paris Area (ESQUIF) measurements, *J. Geophys. Res.*, **108**, D17, <https://doi.org/10.1029/2002JD001561>, 2003.
- 700 Silvern, R. F., Jacob, D. J., Travis, K. R., Sherwen, T., Evans, M. J., Cohen, R. C., Laughner, J. L., Hall, S. R., Ullmann, K., Crouse, J. D., Wennberg, P. O., Peischl, J., Pollack, I. B.: Observed NO/NO₂ ratios in the upper troposphere imply errors in NO-NO₂-O₃ cycling kinetics or an unaccounted NO_x reservoir, *Geophys. Res. Lett.*, **45**, 4466-4474, <https://doi.org/10.1029/2018GL077728>, 2018.
- 705 Tadic, I., Parchatka, U., Königstedt, R., Fischer, H.: In-flight stability of quantum cascade laser-based infrared absorption spectroscopy measurements of atmospheric carbon monoxide, *Appl. Phys. B*, **123**, 146, <https://doi.org/10.1007/s00340-017-6721-z>, 2017.
- Tadic, I., Crowley, J. N., Dienhart, D., Eger, P., Harder, H., Hottmann, B., Martinez, M., Parchatka, U., Paris, J.-D., Pozzer, A., Rohloff, R., Schuladen, J., Shenolikar, J., Tauer, S., Lelieveld, J., and Fischer, H.: Net ozone production and its relationship to nitrogen oxides and volatile organic compounds in the marine boundary layer around the Arabian Peninsula, *Atmos. Chem. Phys.*, **20**, 6769-6787, <https://doi.org/10.5194/acp-20-6769-2020>, 2020.
- 710 Thornton, J. A., Wooldridge, P. J., Cohen, R. C., Martinez, M., Harder, H., Brune, W. H., Williams, E. J., Roberts, J. M., Fehsenfeld, F. C., Hall, S. R., Shetter, R. E., Wert, B. P., and Fried, A.: Ozone production rates as a function of NO_x abundances and HO_x production rates in the Nashville urban plume, *J. Geophys. Res.*, **107**, D12, <https://doi.org/10.1029/2001JD000932>, 2002.
- 715 Tost, H., Jöckel, P., Kerkweg, A., Sander, R., and Lelieveld, J.: Technical Note: A new comprehensive SCAVenging submodel for global atmospheric chemistry modelling, *Atmos. Chem. Phys.*, **6**, 565–574, <https://doi.org/10.5194/acp-6-565-2006>, 2006.
- Tost, H., Jöckel, P., and Lelieveld, J.: Lightning and convection parameterisations – uncertainties in global modelling, *Atmos. Chem. Phys.*, **7**, 4553-4568, <https://doi.org/10.5194/acp-7-4553-2007>, 2007.
- West, J. J., and Fiore, A. M.: Management of tropospheric ozone by reducing methane emissions, *Environ. Sci. Technol.*, **39**, 13, 4685-4691, <https://doi.org/10.1021/es048629f>, 2005.
- 720

- Williams, E. R. and Satori, G.: Lightning, thermodynamic and hydrological comparison of the two tropical continental chimneys, *J. Atmos. Sol.*, **66**, 13-14, 1213-1231, <https://doi.org/10.1016/j.jastp.2004.05.015>, 2004
- Xu, W., and Zipser, E. J.: Properties of deep convection in tropical continental, monsoon, and oceanic rainfall regimes, *Geophys. Res. Lett.*, **39**, L07802, <https://doi.org/10.1029/2012GL051242>, 2012.
- 725 Yienger, J. and Levy II, H.: Empirical model of global soil-biogenic NO_x emissions, *J. Geophys. Res.*, **100**, 11 447–11 464, <https://doi.org/10.1029/95JD00370>, 1995.
- Zahn, A., Weppner, J., Schlote-Holubek, K., Burger, B., Kühner, T., and Franke, H.: A fast and precise chemiluminescence ozone detector for eddy flux and airborne application, *Atmos. Meas. Tech.*, **5**, 363-375, <https://doi.org/10.5194/amt-5-363-2012>, 2012.
- 730 Zanis, P., Monks, P. S., Schuepbach, E., and Penkett, S. A.: The Role of In Situ Photochemistry in the Control of Ozone during Spring at the Jungfrauoch (3,580 m asl) – Comparison of Model Results with Measurements, *J. Atmos. Chem.*, **37**, 1-27, <https://doi.org/10.1023/A:1006349926926>, 2000a.
- Zanis, P., Monks, P. S., Schuepbach, E., Carpenter, L. J., Green, T. J., Mills, G. P., Bauguitte, S., and Penkett, S. A.: In situ ozone production under free tropospheric conditions during FREETEX '98 in the Swiss Alps, *J. Geophys. Res.*, **105**, D19, <https://doi.org/10.1029/2000JD900229>, 2000b.
- 735 Zipser, E. J.: Deep Cumulonimbus Cloud System in the Tropics with and without Lightning, *Mon. Wea. Rev.*, **122**, 1837-1851, [https://doi.org/10.1175/1520-0493\(1994\)122<1837:DCCSIT>2.0.CO;2](https://doi.org/10.1175/1520-0493(1994)122<1837:DCCSIT>2.0.CO;2), 1994.